J. Cent. South Univ. (2022) 29: 898−911
DOI: https://doi.org/10.1007/s11771-022-4954-4

Springer

Microstructure and mechanical properties of 6061 aluminum alloy laser-MIG hybrid welding joint

FAN Cong(范聪)[1], YANG Shang-lei(杨尚磊)[1, 2]*, DUAN Chen-feng(段晨风)[1],

ZHU Min-qi(朱敏琪)[1], BAI Yi-shan(白易山)[1]

1. School of Materials Engineering, Shanghai University of Engineering Science, Shanghai 201600, China;
2. Shanghai Collaborative Innovation Center of Laser Advanced Manufacturing Technology, Shanghai 201600, China

Abstract: In this paper, 3 mm 6061 aluminum alloy sheets were welded by laser MIG hybrid welding. Based on the experiment, the best welding parameters were determined to ensure the penetration welding. The detailed microstructure, tensile and fatigue fracture morphology and surface fatigue damage of the welded joints were analyzed by optical microscope (OM), scanning electron microscope (SEM) and energy dispersive spectrometer (EDS). The results show that there are two main kinds of precipitates, one is the long Si rich precipitates at the grain boundaries, the other is the intragranular Cu rich precipitates. The tensile test results show that the tensile strength of the joint is 224 MPa, which is only 70.2% of the base metal. Through the analysis of tensile fracture, there are great differences in the formation of tensile dimple. In the tensile-tensile fatigue test with a stress rate of 0.1, the conditional fatigue limits of base metal and welded joint are 101.9 MPa and 54.4 MPa, respectively. By comparing the fatigue fracture of the welded joints under different stress amplitudes, it was found that the main factor leading to the fracture of the joint is porosity. Through further analysis of the pore defects, it was found that there are transgranular and intergranular propagation ways of microcracks in the pores, and the mixed propagation way was also found.

Key words: aluminum alloy; laser-MIG hybrid welding; fatigue property; microstructure; mechanical properties

Cite this article as: FAN Cong, YANG Shang-lei, DUAN Chen-feng, ZHU Min-qi, BAI Yi-shan. Microstructure and mechanical properties of 6061 aluminum alloy laser-MIG hybrid welding joint [J]. Journal of Central South University, 2022, 29(3): 898−911. DOI: https://doi.org/10.1007/s11771-022-4954-4.

1 Introduction

The demand for high-strength, lightweight materials in modern aviation, automotive, and high-speed rail manufacturing is increasing due to energy consumption around the world [1]. 6xxx series heat-treated aluminum alloys, represented by 6061 aluminum alloy, have been widely used in aircraft, high-speed rail, and other structural parts due to its high specific strength, high corrosion resistance and good weld ability [2 − 4]. In the manufacturing process of this kind of structure, welding is the preferred connection process. The fusion welding technology represented by MIG welding has become the first choice among many welding processes because of its mature process and low cost [5]. However, some studies have shown that

Foundation item: Project(51971129) supported by the National Natural Science Foundation of China; Project(19ZR1421200) supported by the Shanghai Natural Science Foundation, China
Received date: 2021-05-06; **Accepted date:** 2021-09-16
Corresponding author: YANG Shang-lei, PhD, Professor; Tel: +86-17717330632; E-mail: yslyangshanglei@163.com; ORCID: https://orcid.org/0000-0003-2190-9267

MIG welding is characterized by large heat input and slow welding speed. During the welding process, there will be obvious defects such as severe softening of heat affected zone (HAZ) and large welding deformation, which have adverse effects on the mechanical properties and fatigue properties of joints [6 − 8]. Compared with MIG welding, laser welding has the advantages of high welding efficiency, small heat input and small deformation. However, the characteristics of aluminum alloy materials determine that there are many low melting points of alloy components, and the evaporation is large during laser welding, which is prone to porosity defects and burning loss of alloy elements [9].

In order to improve the deficiencies of these two welding processes, STEEN [10] proposed laser-MIG hybrid welding, which is a new welding method with high efficiency of heat source combining the advantages of laser welding and MIG welding [11]. Compared with single heat source welding technology, laser-MIG hybrid welding has higher energy density and better heat source quality. Under the synergistic action of hybrid heat source, welding joints have strong bridging ability, high welding stability and high welding quality [12−14]. In addition, the welding efficiency of laser-MIG hybrid welding is 3−4 times higher than that of pure MIG welding [15]. PAIL [16] used three different laser welding methods to weld 6061 aluminum alloy. Through comparison, he found that laser-MIG welding had the best weld bead forming, and the introduction of arc greatly reduced the clamping accuracy of butt welding parts and improved the production efficiency. However, due to the influence of oxide film on the surface of aluminum alloy and evaporation of low melting point elements at high temperature, the problem of laser-MIG hybrid welding pores is difficult to avoid [17].

At present, laser-MIG hybrid welding has attracted worldwide attention due to its breakthrough advantages. However, most of the researches focus on the optimization of welding parameters and the formation mechanism of defects (porosity and undercut) [18 − 20]. There are relatively few reports on the mechanical properties of welded joints, especially the fatigue properties. Fatigue damage is the most common failure mode of welded joints in actual service, even for the welded bead without obvious defects [21]. Studies have shown that fatigue cracks would first crack at pores in welded joints of aluminum alloys [22−24]. The existence of pores would reduce the actual load area inside the welded joints, resulting in fatigue failure of the welded structure in a low stress range [25]. It is well known that the service of 6061 aluminum alloy welded structure is a long-term process, so it is necessary to analyze the fatigue performance of 6061 aluminum alloy laser-MIG hybrid welded joints.

In this work, the 6061-T6 aluminum alloy sheets with 3 mm thickness were welded by laser-MIG hybrid welding. The microstructure and mechanical properties of welded joints were analyzed. The research results have important practical value for the further study of laser-MIG hybrid welding technology of 6061 aluminum alloy.

2 Materials and experiments

2.1 Material and welding process

The base metal (BM) used in this work is a 3 mm thick 6061-T6 aluminum alloy. According to its chemical composition, it is prone to hot cracks. In order to reduce this crack tendency, ER4043 with a diameter of 1.2 mm was used. Chemical compositions of BM and welding wire are shown in Table 1. Before welding, the surface of the BM is treated by mechanical grinding to remove the oxide film on the surface to prevent welding defects in the welding process. Figure 1 shows the schematic diagram of laser-MIG hybrid welding of 6061-T6 aluminum alloy. The laser system is composed of YLS-5000 fiber laser from IPG Photonics, KR60HA six-axis robot from KUKA, and KEMPARC450 MIG welding machine from KEMPPI. During welding, the laser is in the front and the arc is in the back. The angle between the laser and the welding torch and the aluminum alloy plate is 80° and 60° respectively, and the argon gas (99.999%) is used as the protective gas. The welding process parameters used in the welding test are shown in Table 2. After welding, the welded joints were cooled at room temperature, and the samples for tensile tests and fatigue tests were cut from the plates, and the weld reinforcement of the sample for test was processed after cutting. The sample cutting and size diagrams are shown in Figure 2.

Table 1 Chemical composition of base metal and welding wire (wt%)

Element	6061	ER4043
Mg	0.5	≤0.05
Si	0.6	5
Zn	≤0.20	≤0.10
Fe	≤0.35	≤0.80
Cu	≤0.30	≤0.30
Mn	≤0.50	≤0.05
Cr	≤0.30	—
Ti	≤0.10	≤0.2
Al	Bal.	Bal.

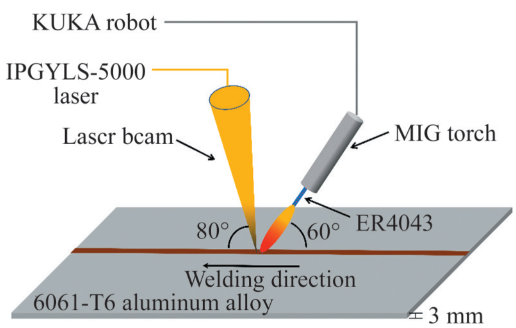

Figure 1 Schematic diagram of welding process

Table 2 Welding parameters

Parameter	Value
Laser power/kW	3
Current/A	131
Voltage/V	18.1
Wire feeding rate/(m·min^{-1})	8
Welding speed/(mm·s^{-1})	25
Defocusing amount/mm	−1

2.2 Microstructure characterization

According to GB/T3246.1—2012 standard, the surface of the sample was polished until no obvious scratches were found, and then the metallographic sample was prepared by etching with Keller reagent (V(HF): V(HCl): V(HNO_3) =1: 1.5: 2.5). VHK-600 optical microscope (OM) and S-3400N scanning electron microscope (SEM) were used to observe the metallographic sample.

2.3 Tensile tests and fatigue tests

According to GB/T2651—2008 standard, tensile tests were carried out on the base metal (BM) and laser-MIG welded joints (WJ) at 1 kN/min. In order to ensure the accuracy of tensile data, the average value of three groups of tensile tests was taken as the test result.

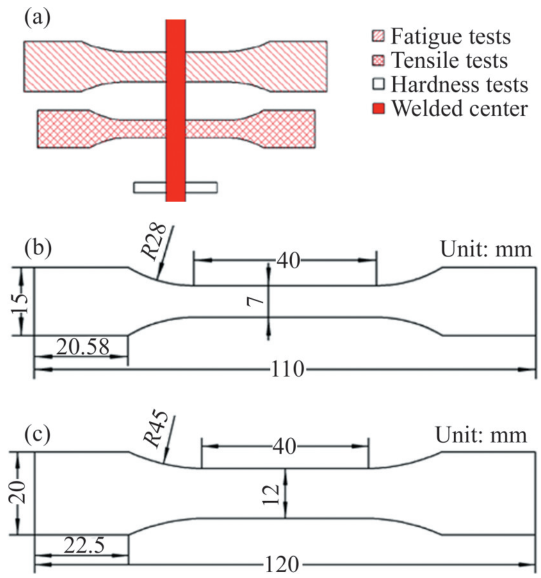

Figure 2 Interception positions of metallographic, fatigue and tensile specimens (a), the size of tensile specimens (b) and fatigue specimens (c)

According to the GB/T26077—2010 standard, the fatigue tests were carried out at room temperature ((25±3) °C) and relative humidity (40%−60%) by symmetrical tension−tension cycle with sinusoidal loading waveform until the specimen reached 1×10^6 cycles or fracture. The stress ratio ($R=\sigma_{min}/\sigma_{max}$) and load frequency were 0.1 and 15 Hz, respectively. All fatigue specimens were cyclic loaded under different stress amplitudes ($\Delta\sigma=\sigma_{max}-\sigma_{min}$). The ultimate fatigue strength ($N_f\geq10^6$) of BM and WJ was analyzed by S-N fitting curve.

All the tensile and fatigue tests were carried out on the Zwick/Roell Amsler HB250 hydraulic servo material testing machine, and the tensile and fatigue fractures were observed and analyzed by S-3400N and TESCAN-VEGA3 scanning electron microscope (SEM).

3 Test results

3.1 Microstructure of 6061 aluminum alloy laser-MIG welded joint

Figure 3 describes the OM images of HAZ and BM in the welded joint. HAZ1 in Figure 3 is the HAZ microstructure near BM, while HAZ2 is close to the weld bead. BM structure in Figure 3(a) is obviously long strip, which is typical rolled structure. The average size of grains marked with

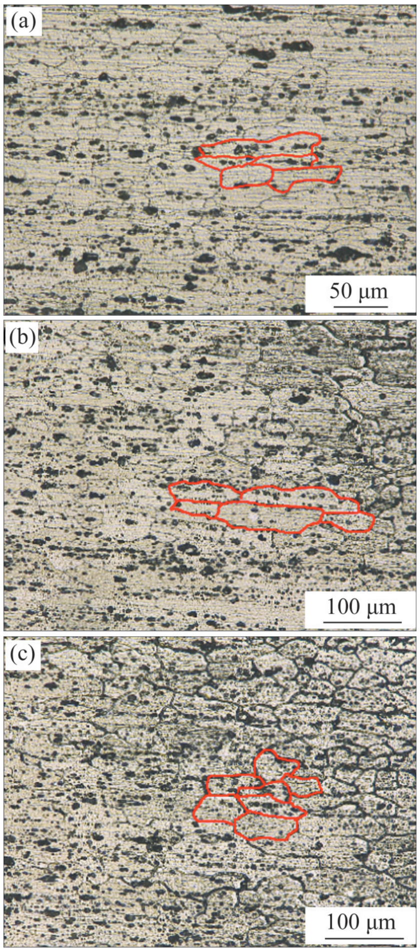

Figure 3 Microstructures of optical microscope (OM): (a) BM; (b) HAZ1; (c) HAZ2

red lines in Figure 3 was calculated, and the results are shown in Table 3. The results show that the grain length and width of HAZ1 near BM are coarsened obviously, but the aspect ratio remains unchanged. HAZ2 near welding zone (WZ) has obvious coarsening only in width, and its grain morphology is different from that of BM and HAZ1, which is granular and close to the as-cast structure. The grains in HAZ2 are close to the weld bead, which is greatly affected by the heat source. The temperature at this position during welding would exceed the solidus temperature of BM, and the grain partially melts and forms granular as-cast structure during the subsequent cooling process. However, HAZ1 is far away from the weld bead, the welding temperature could not reach the solution temperature, but exceeds the overaging temperature of the alloy, and the grains coarsen at high temperature.

Table 3 Grain sizes of HAZ1, HAZ2 and BM marked in Figure 3

Sample	Length/μm	Width/μm	Length-width ratio
BM	61.4	14.7	4.18
HAZ1	95.1	20.8	4.57
HAZ2	60.9	24.1	2.53

Figure 4(a) depicts the macroscopic morphology of the weld bead taken by OM. It can be seen from the figure that the weld bead is well formed without defects such as undercut and penetration. Four locations were selected in Figure 4(a) to analyze the microstructure of the weld bead as shown in Figures 4(b), (c), (d) and (e). It can be seen from Figures 4(b), (c) and (d) that the weld bead grains are mainly fine equiaxed grains with uniform grain size and irregular distribution. There are obvious snowflake equiaxed crystals in the weld bead. During the welding process, due to the large undercooling in the molten pool, the suspended free crystals in the molten pool can directly nucleate in the liquid metal, and are less constrained by the surrounding, and diverge around to form snowflake-like equiaxed crystals [23]. The microstructure of grains in different areas of weld bead is mainly affected by the combined action of temperature gradient (G) and solidification rate (R) [26].

During the welding process, the center of the molten pool had the highest temperature, but the edge of the molten pool was close to BM, the heat dissipation was fast, and the temperature gradient was high, which resulted in a lower temperature at this location. At the same time, the solidification rate near the fusion line was low, so the G/R was large. Under the action of component supercooling, the grains grew to the center of the molten pool with columnar dendrites, as shown in Figure 4(b) red virtual coil. Because the welding energy density is high, the molten pool center has higher temperature with low cooling rate, the temperature gradient G decreases, and at the same time the crystallization rate R increases, so G/R of weld center decreases, and composition of supercooling increases gradually. Consequetly, the quick growth of columnar dendrites was restrained, the isometric and small dendrites began to appear in weld center, until the liquid metal in the molten pool was firm. It can be seen from Figure 4(b) that the microstructure on both sides of fusion line was disorderly, mainly

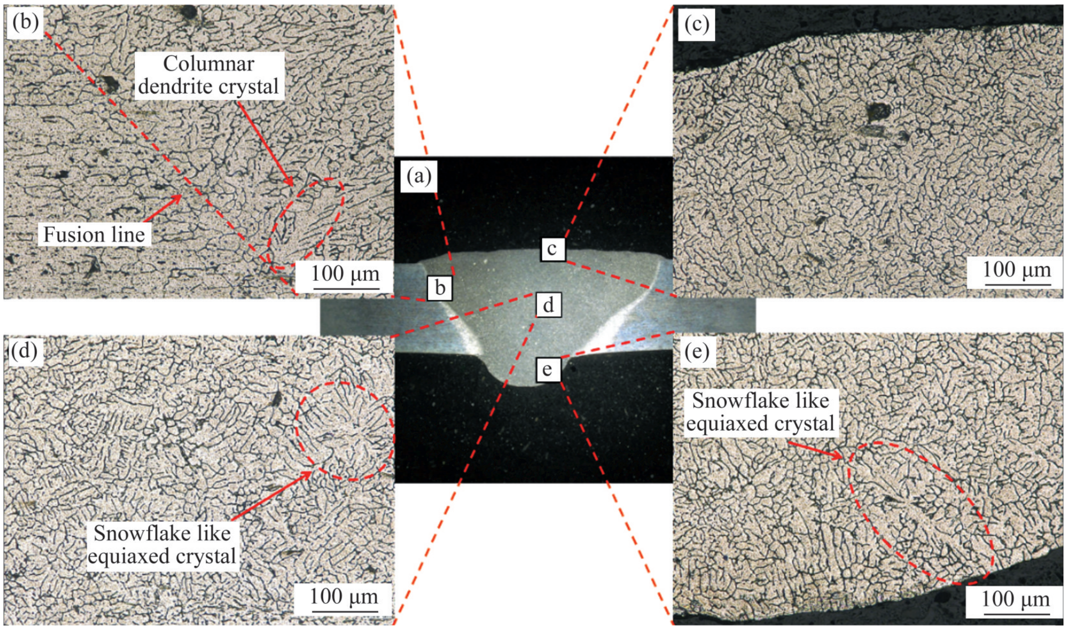

Figure 4 Morphology of the weld bead taken by OM: (a) Macro morphology of weld bead; (b) Microstructure of fusion zone; (c) Microstructure of the upper part of weld bead; (d) Microstructure of the middle part of weld bead; (e) Microstructure of the lower part of weld bead

including fine equiaxed grains, columnar dendrites, heat-affected zone granular grains and semi-fused grains. The grains morphology on both sides of the fusion line is very different. Although the vicinity of the fusion line was a relatively narrow area on the scale, the strong microstructure heterogeneity would still cause great differences in mechanical properties, which made it impossible for different micro-regions to coordinate deformation under load, thereby affecting the strength of welded structural parts.

SEM observation was performed on the microstructure of the weld bead and fusion line, as shown in Figure 5. There are many second phase particles distributed in the dark aluminum matrix in the weld bead, which are unevenly distributed in the grain boundary or inside the grain. The same secondary phase particles distribution can be clearly observed near the fusion line. From the morphology of these particles, it can be found that the precipitates at the grain boundary are mostly long strips, while the precipitates inside the grains are obviously spherical. EDS analysis was performed for the partially numbered second phases in Figures 5(b), (d) and (e), and the results are shown in Table 4. According to the results, the content of Cu element in the precipitates numbered 3, 4, 7 is relatively high, and the content fluctuates between 4.52% and 9.92%. However, the content of Si element in the elongated strip precipitates at grain boundaries is relatively high, which fluctuates between 23.32% and 29.17%. In addition, by comparing the composition of BM in Table 1, it can be found that the content of Mg element in these precipitated phases is low. This is because the weld center temperature was much higher than the boiling point of magnesium (1090 °C) in the welding process, resulting in the decrease of Mg content [27].

3.2 Tensile test results

The average tensile properties of BM and WJ are shown in Table 5. The engineering stress−strain curves of BM and WJ are shown in Figure 6. It can be seen from Table 5 that compared with BM, the elongation and strength of WJ are significantly decreased. The tensile strength (TS), yield strength (YS) and elongations of WJ and BM were 224 MPa and 319 MPa, 132 MPa and 287 MPa, 3.1% and 13.3%, respectively. It can be seen from Figure 6(a) that the tensile fracture of BM is about 45° from the tensile stress direction, which is a typical blade fracture. The tensile fracture surface of the welded joint in Figure 6(b) indicates that the fracture of the joint does not show obvious ductile fracture

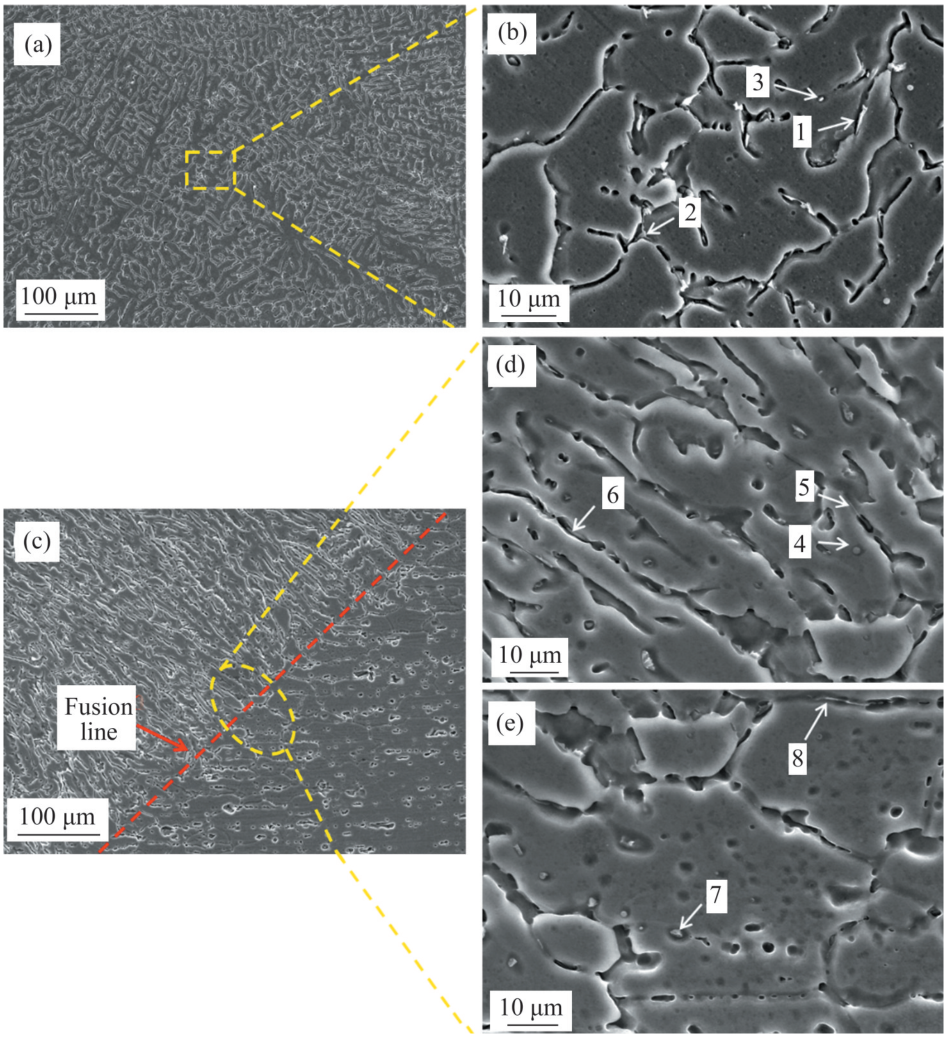

Figure 5 (a) SEM images of weld bead; (b) Local enlarged view of Figure5(a); (c) SEM image of fusion line; (d) and (e) Local enlarged view of Figure 5(c)

Table 4 EDS results of different precipitate phases marked in Figure 5

Location	x(Al)/%	x(Mg)/%	x(Si)/%	x(Cu)/%
1	70.15	0.50	29.17	0.18
2	73.48	0.92	25.08	0.52
3	77.38	1.65	16.45	4.52
4	72.61	1.40	16.07	9.92
5	73.66	1.91	23.32	1.11
6	72.30	0.82	25.69	1.19
7	72.22	1.13	18.01	8.64
8	69.75	1.32	27.69	1.24

Table 5 Tensile test results of BM and WJ

Sample	Tensile strength/MPa	Yield strength/MPa	Elongation/%
BM	319	287	13.3
WJ	224	132	3.1

characteristics. Figure 6(b) shows that the tensile fracture of WJ is located in the welded center and accompanied by porosity defects. The existence of pores will not only reduce the actual bearing area of the joint, but also induce secondary cracks during loading, as shown in Figure 6(c).

Figure 7 shows the SEM image of tensile fracture of BM. Figures 7(a) and (b) show regular dimples with a size of about 20 μm. The dimples with this morphology are standard equiaxial dimples [28]. The dimples shown in Figure 7(b) were formed when the dispersed phases gradually detached from the matrix and grow into micropores when subjected to tensile stress. In the dimples, some remnants of broken second-phase particles can be observed. According to EDS result (Figure 7(c)), the second phase particles in the dimple can be judged as β phase [29]. Figure 8 shows the tensile

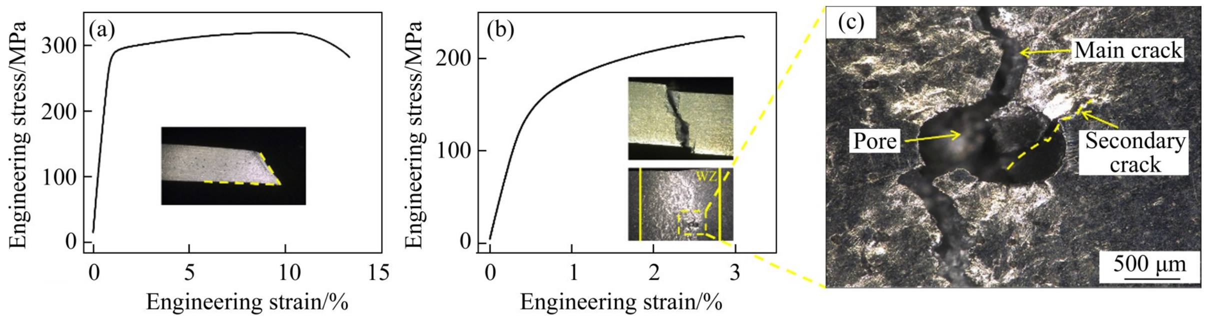

Figure 6 (a) Stress−strain curve of BM; (b) Stress−strain curve of WJ; (c) OM enlarged view of pore defect in Figure 6 (b)

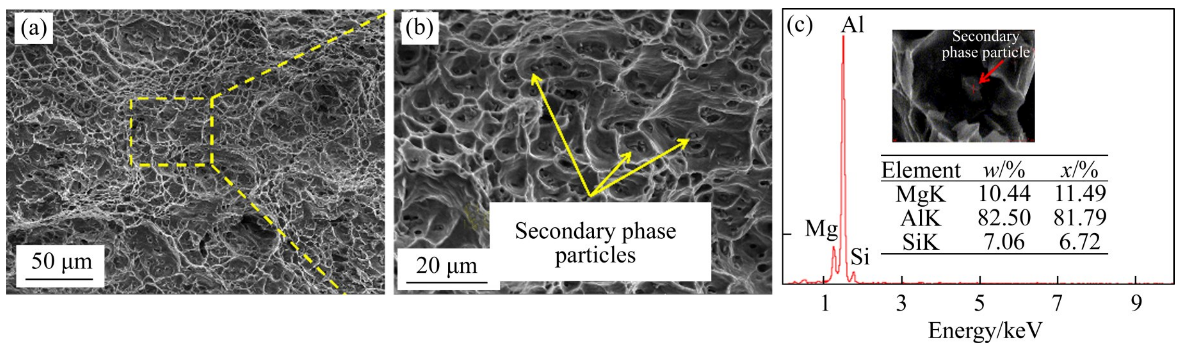

Figure 7 (a) SEM images of BM tensile fracture; (b) Local enlarged view of Figure 7(a); (c) EDS results of the second phase particles in dimples

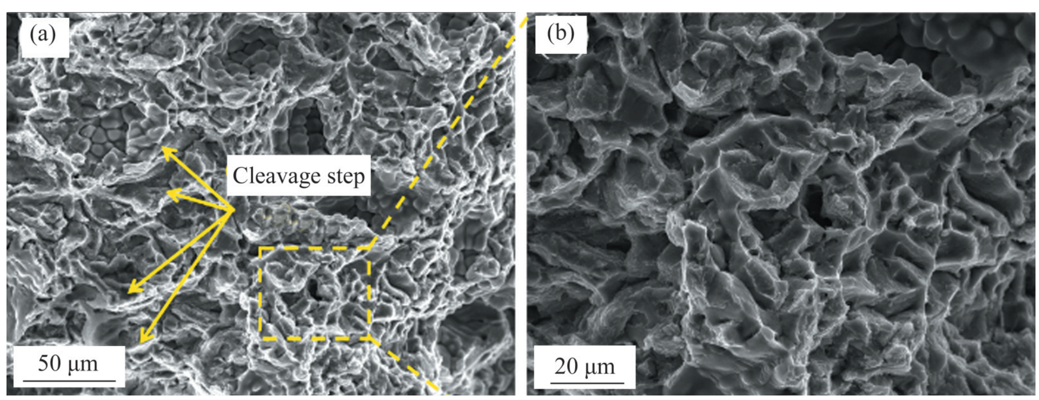

Figure 8 (a) SEM image of WJ tensile fracture; (b) Local enlarged view of Figure 8(a)

fracture of 6061 aluminum alloy laser-MIG hybrid welded joint. It can be found from Figures 8(a) and (b) that the dimple morphology of WJ tensile fracture is broken, which is different from BM. Since the ER4043 welding wire was selected in this test, and its main alloy components are Al and Si, there were few precipitation particles at the weld bead after welding, leading to different forming modes of WJ dimples. The tensile dimples of the joint were mainly due to the formation of voids in the joint under the action of tensile normal stress. The voids grew up along all directions in the space under the external force, and finally the dimple morphology appeared in the fracture. A large number of dimples distributed indicate that the joint has a certain plasticity, but some cleavage steps can be observed in Figure 8(a). The low elongation of the joint in Table 5 indicates that the joint has a certain brittleness during the tensile process. In conclusion, the tensile fracture mode of 6061 aluminum alloy laser-MIG hybrid welding joint is ductile-brittle mixed fracture.

3.3 Fatigue test results

Basquin's formula [30] was used to fit the data obtained from the fatigue test of BM and WJ. The formula after fitting is shown as Eqs. (1) and (2). Equation (1) is the fitting formula of WJ and equation (2) is the fitting formula of BM and the fitting curve obtained is shown in Figure 9.

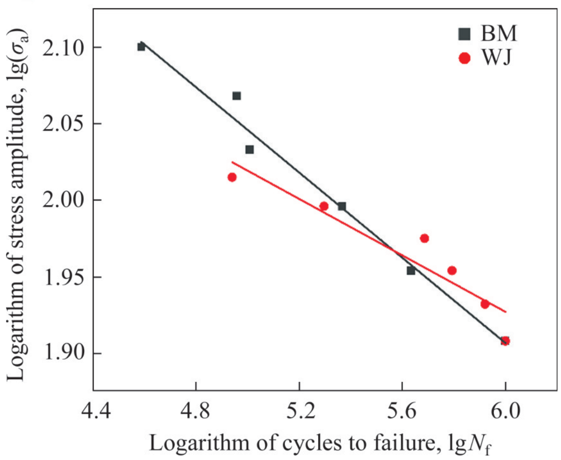

Figure 9 Fatigue test data and fitting curve of WJ and BM

$$\lg\Delta\sigma=2.38753-0.1086\lg N \quad (1)$$

$$\lg\Delta\sigma=2.78956-0.1302\lg N \quad (2)$$

According to Eq. (1) and Eq. (2), the slope of BM fitting curve is slightly smaller than that of WJ, which indicates that the fatigue life of BM decreases faster with the increase of stress level. At the same time, under the condition of 1×10^6 cycles, the fatigue limits of BM and WJ are 101.9 MPa and 54.4 MPa respectively, and the fatigue life of WJ is only 53.4% of that of BM. It is worth noting that under different stress amplitudes, the welded joint samples all fractured at the weld bead, indicating that the weld bead has the lowest strength of the joints, which is consistent with the tensile test results.

Figure 10 shows the OM image of fatigue fracture path of welded joint. It can be seen from the figure that the crack initially nucleates near the fusion line. Under the action of the driving force of the crack tip, the fatigue crack propagates in a *Z*-shaped way, and there is obvious plastic deformation near the crack. Studies have shown that fatigue cracks would initiate at the surface or near surface defects of the specimen, resulting in failure under low stress [22, 31]. Figure 11 shows the fatigue fractures with the stress amplitude of 99, 94.5, 90 and 85.5 MPa. It can be seen from the figure that the porosity defect located on the surface

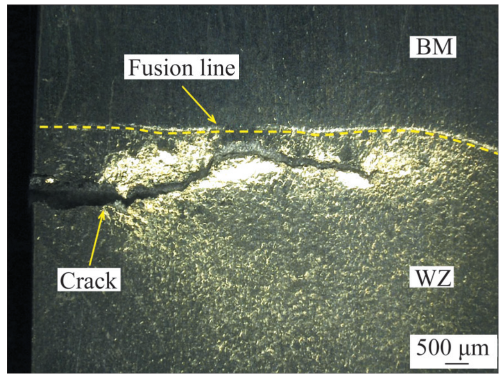

Figure 10 OM image of fatigue fracture path of welded joint

or near the surface is the main reason for the fracture of the hybrid welded joints. In addition to the small-size pore in Figure 11(b), the pores leading to fatigue cracks initiation under other stress amplitude are all large. The pores with regular shape are considered to be caused by the evaporation of Mg element with low boiling point in BM and the oxide film on BM surface [27]. When fatigue test was carried out, the stress near the edge of the pores was much greater than the fatigue stress, which made the fatigue cracks easily initiate and propagate from the pores. It is noteworthy that according to ZHAO et al [32], due to the rapid cooling rate of the welding pool, the small pores that cannot be escaped in time in the welding pool would accumulate large-scale pores at the root of the weld bead, which explains that the large pores in the fatigue fractures were mostly located on the near surface of the specimen.

Figure 12 shows the fatigue fracture of the sample with the stress amplitude of 85.5 MPa after 834052 cycles. As can be seen from Figure 12(a), after the fatigue test of the sample, the two closely connected 1 mm pores were the main reason for the initiation of fatigue cracks. The connected pores create a coupling effect on the stress field around the defect, thus further enlarging the stress concentration at this position [33]. After the initiation of the fatigue crack at the pores, the fatigue crack would enter a stage of stable expansion under the action of external stress, as shown in region II in Figure 12(a). The crack in region II began to expand around after cracking at the pores (as shown by the red arrows), and the area of region II was large, indicating that the crack

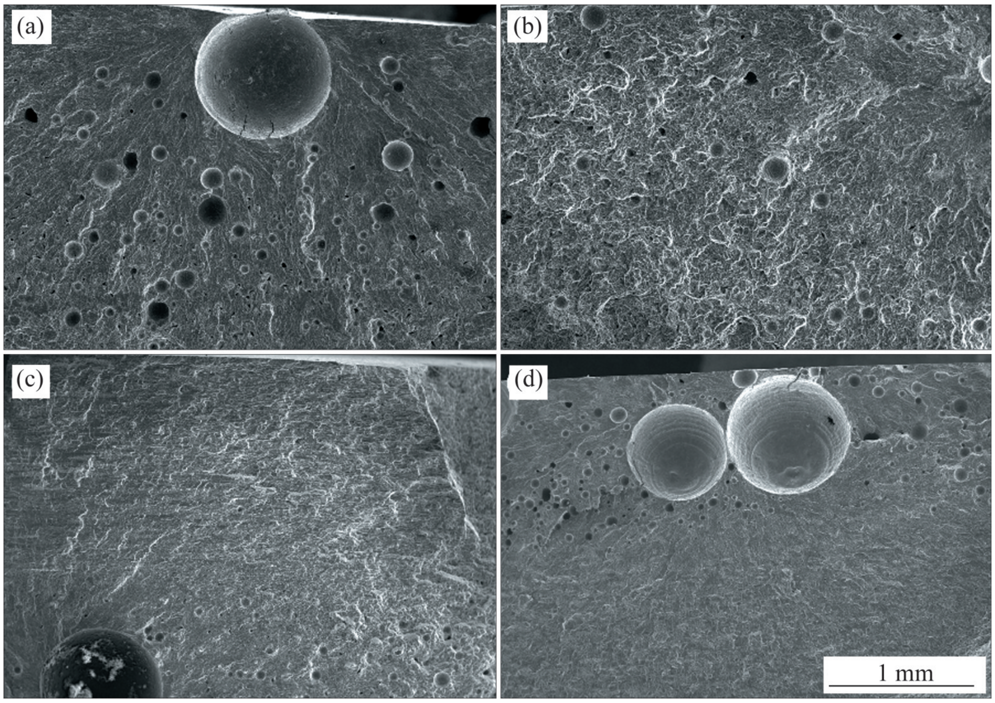

Figure 11 SEM images of fatigue crack sources under different stress amplitudes: (a) $\Delta\sigma$=99 MPa, N=198378; (b) $\Delta\sigma$=94.5 MPa, N=485937; (c) $\Delta\sigma$=90 MPa, N=621441; (d) $\Delta\sigma$=85.5 MPa, N=834052

propagation stage occupied a large part in the whole process of specimen fracture. The III region in Figure 12(a) is the transient fracture zone of the sample. The fatigue sample would fracture instantaneously after the fatigue stable expansion stage (the square zone), which took a very short time and was completed almost instantaneously. Figure 12(b) is an enlarged view of the yellow box in Figure 12(a). The red arrows in the figure are the propagation direction of the fatigue crack. The propagation direction of the crack was not fixed, but the morphology of the fracture extending in different directions was the same. This is the brittle fracture caused by the fracture of the material in a specific and determined lattice plane under the condition of tensile stress. In Figure 12(b), a large number of ridge-like morphology (in the yellow dotted line box) can be seen, and the direction of these ridge-like patterns is consistent with the propagation direction of fatigue crack. The ridge-like patterns were formed mainly due to the fatigue crack propagated on different cleavage planes, when two different propagation planes intersected, the ridge-like pattern in Figure 12(b) would be produced. Figure 12(c) is the enlarged figure of Figure 12(b). In Figure 12(c), fractures with river pattern and ridge pattern also appear. The fatigue crack was formed when different lattice planes were staggered during the opening of different lattice planes. A large number of fatigue strips can be seen in Figure 12(c) (shown by yellow arrows in Figure 12(c)). From the figure, it can be seen that fatigue strips were in many different directions, which was due to the obstruction of grain boundaries when fatigue cracks propagated, resulting in different directions of fatigue cracks propagating in different grains, and ultimately leading to different directions of fatigue strips.

Figure 12(d) is an enlarged view of region III in the fatigue fracture, from which a large number of dimples can be observed, with a morphology similar to that of the tensile fracture of WJ. Figure 12(e) shows the secondary cracks generated by dimples in the fracture. The secondary cracks were perpendicular to the fracture generated during fatigue tests. Figure 12(f) is an enlarged view of the inside of the dimples. Obvious slip bands can be observed in the figure, which were caused by plastic deformation as the dimples grew, and a large number of small microscopic cavities can be observed, which were factors contributing to the dimple formation.

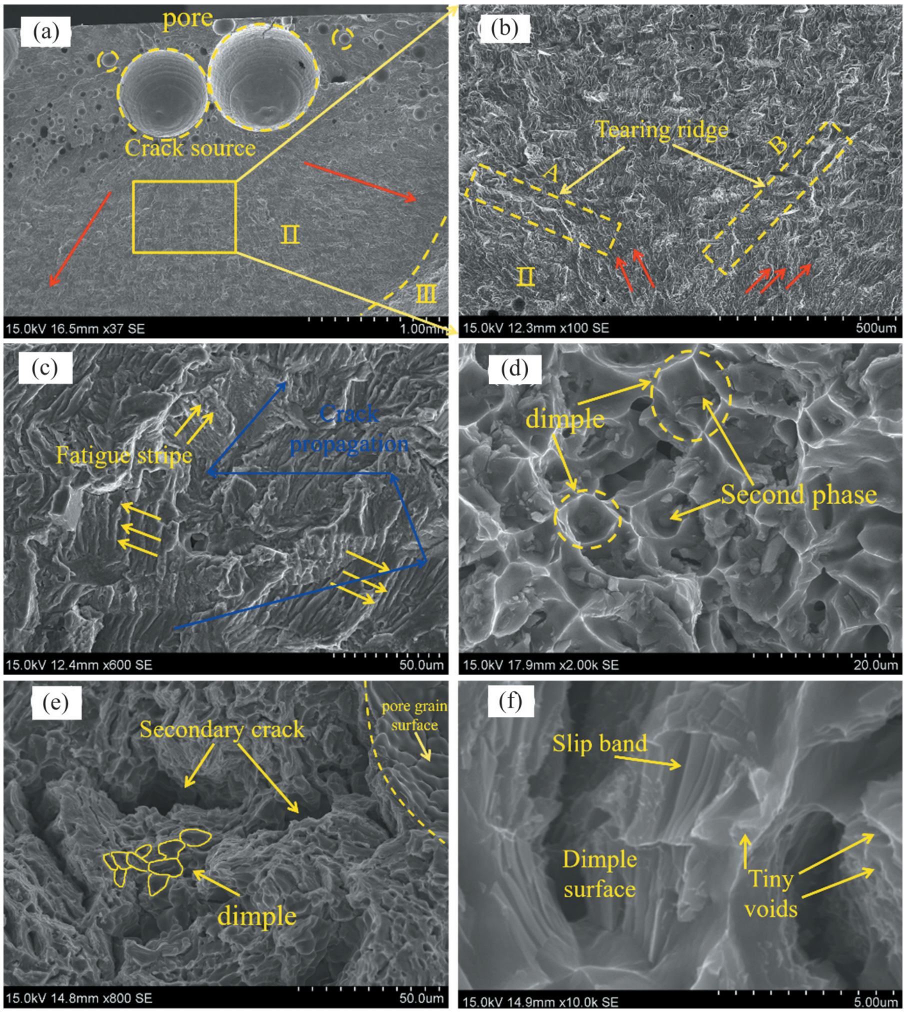

Figure 12 SEM images of fatigue fracture of welded joints: (a) Pores under weld surface; (b) Crack propagation zone; (c) Fatigue strip; (d) Instantaneous fracture zone; (e) Secondary crack; (f) Dimple

4 Discussion

According to the above analysis, it can be found that the main cause of fatigue fracture is the existence of pores. Figure 13 shows the SEM images of the surface of the welded joints under different loading stress. It can be seen from the figure that the regular slip bands can be clearly observed on the surface of the joint under higher stress, but the slip bands cannot be observed on the surface of the joint under lower stress. This indicates that the low stress is not enough to form enough slip bands on the surface, which makes the traditional surface intrusion extrusion mechanism [34] not the main cause of fatigue crack initiation of welded joints under low stress. Therefore, it can be considered that the origin of fatigue crack is transferred from the surface to the interior. After a certain cyclic loading, the internal discontinuous region where the pores are located falls off from the matrix interface, resulting in the initiation of microcracks at the pores. Secondly, due to the existence of pores, the geometric conditions of the specimen are not continuous, and a serious stress concentration phenomenon is formed at the edge of the pores. The stress at the edge of the pores is much higher than the applied stress, which makes the slip bands easier to form at the edge of the pores, initiate cracks, and reduce the fatigue life of the specimen, as shown in Figures 13(c) and (d). By further observation of the fracture pores, two kinds of microcracks propagation modes were found. One is intergranular cracking at the edge of the pores, the other is transgranular fracture.

When the welded joint was subjected to cyclic loading, it was easier to produce cyclic slip inside

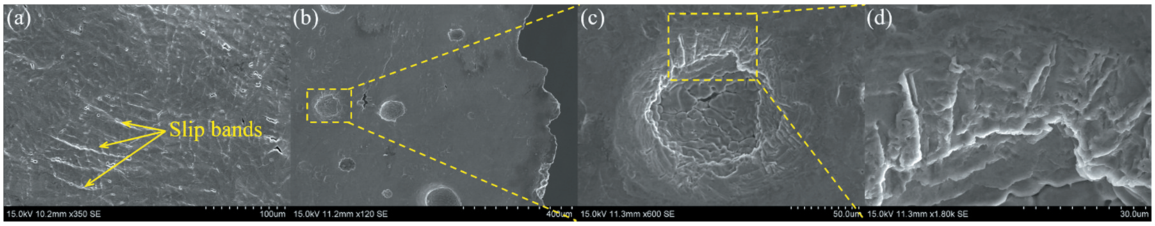

Figure 13 (a) SEM image of joint surface under $\Delta\sigma$=99 MPa; (b) SEM image of joint surface under $\Delta\sigma$=85.5 MPa; (c) Partial enlarged image of (b); (d) Partial enlarged image of (c)

the grains, which promoted the fatigue microcracks to propagate in a transgranular manner, as shown in Figure 14. A pore can be observed in the upper right corner of Figure 14(a), and the grains inside the pore are clearly visible. There are obvious cleavage steps and microcleavage surfaces at the edge of the pore. Microcracks may form simultaneously in multiple parts of pores and propagate along different planes. When different cleavage planes intersect, the cleavage steps shown in the figure would be generated. The existence of cleavage planes and cleavage steps is the typical characteristic of brittle fracture, which indicates that this brittle fracture exists at the edge of pores. When cleavage fracture occurs, the fatigue crack is usually transgranular propagation [28]. In addition to extending outward along the edge of the pores, the transgranular fracture also extended towards the interior of the

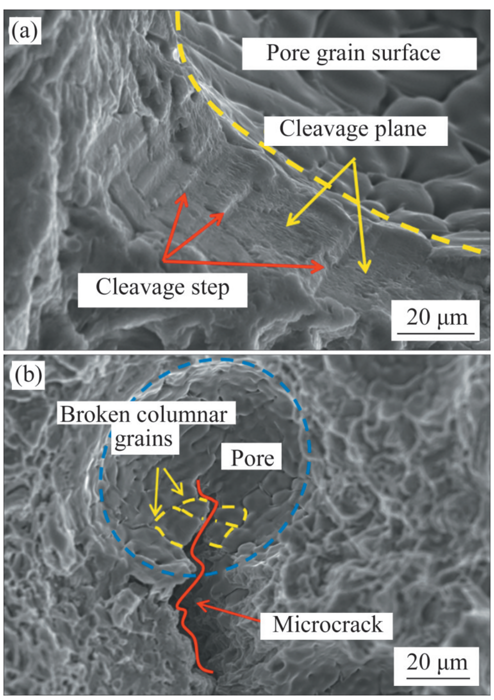

Figure 14 SEM images of pore transgranular crack: (a) Cleavage step; (b) Transgranular crack

pores, as shown in Figure 14(b). An obvious microcrack (shown in the red curve) can be observed in the figure. The crack initiated at the edge of the pores and continued to expand towards the interior of the pores. The microcracks were observed to pass through two complete grains (yellow dotted lines) about 30 μm in length but only about 10 μm in width.

In very few cases, the microcracks at the pores would propagate along the grains. It is generally considered that grain boundary is one of the important factors of materials strengthening since the bond force at the grain boundary is greater than that in the grain, so the microcracks propagation along the grain indicates the weakening of grain boundary. The segregation of solute elements on the grain boundary of metallic materials is considered to be an important reason for the nucleation and propagation of intergranular microcracks. Figure 15 shows a schematic diagram of the intergranular crack at the pore, located near the fusion line of the welded joint. It is clear from the figure that the crack propagated along the equiaxed grains within the pore. According to the precipitate analysis at the fusion line in Table 4, there are many solute elements at the grain boundaries. Their segregation at grain boundaries would reduce the bonding energy of grain boundaries, and the decrease of bonding strength would lead to the decrease of local effective fracture work, which would eventually lead to the decrease of fracture toughness of the sample. Therefore, when the solute elements at the grain boundaries reach a certain level, the microcrack will propagate along the grain boundaries, and the corresponding critical value depends on the yield strength, grain size and microstructure of the material [28].

In addition to the single microcracks intergranular propagation, a mixed mode of

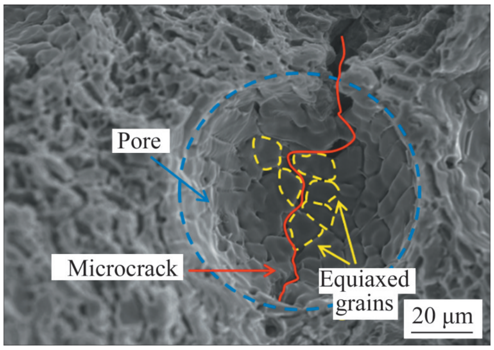

Figure 15 SEM image of intergranular crack at pore

microcracks intergranular and transgranular propagation was found at the fusion line, as shown in Figure 16. After the initiation of the microcrack in the figure, it first propagated along the grain boundaries of the grains marked by the yellow dotted line. Due to the complex grain types near the fusion line, there were not only fine equiaxed grains, but also long columnar grains. When the microcrack propagated into columnar grains, the energy consumption of propagation along grain boundaries was much greater than that of transgranular mode [22]. At this point, the microcrack would choose the transgranular way to expand.

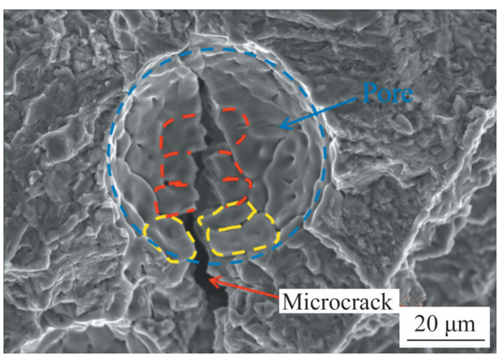

Figure 16 SEM image of mixed propagation of microcrack at pore

5 Conclusions

In this work, tests of the microstructure, tensile and fatigue behavior of 6061-T6 aluminum alloy laser-MIG hybrid welded joints were conducted. The conclusions are as follows:

1) Under the influence of welding thermal cycle, the HAZ structure near BM is coarsened obviously, but the morphology is still like BM long strip; The HAZ structure near the weld is granular. The microstructure of the weld center is mainly single equiaxed crystal, while the microstructure near the fusion line is complex. There are two main kinds of precipitates, one is the long Si rich precipitates at the grain boundaries, the other is the intragranular Cu rich precipitates.

2) The tensile strength of welded joint and base metal is 224 MPa and 319 MPa, respectively. There are a large number of dimples on the tensile fracture surface of the welded joint and the base metal, but their morphology and size are different due to the different formation ways.

3) Under the conditional fatigue life of 1×10^6 cycles, the conditional fatigue strength of the welded joints and the base material is 54.4 MPa and 101.9 MPa, respectively. By comparing the fatigue fracture morphology of welded joints under different stress amplitudes, it is found that the large porosity near the surface is the main cause of joint failure.

4) Further analysis of the pores in the fatigue fracture shows that the microcracks at the pores have both intergranular and transgranular propagation modes, and the mixed propagation modes of the two have also been found.

Contributors

FAN Cong was responsible for experiments and paper writing; YANG Shang-lei conducted the literature review; DUAN Chen-feng, ZHU Min-qi and BAI Yi-shan were in charge of the whole trial. All authors read and approved the final manuscript.

Conflict of interest

The authors declare that they have no known competing financial interests or personal relationships that could have appeared to influence the work reported in this paper.

References

[1] ZHANG Jin-liang, YE Jie-liang, SONG Bo, et al. Comparative study on microstructure and electrochemical corrosion resistance of Al7075 alloy prepared by laser additive manufacturing and forging technology [J]. Journal of Central South University, 2021, 28(4): 1058−1067. DOI: https://doi.org/10.1007/ s11771-021-4679-9.

[2] YAN Shao-hua, XING Bo-bin, ZHOU Hai-yang, et al. Effect of filling materials on the microstructure and properties of

hybrid laser welded Al-Mg-Si alloys joints [J]. Materials Characterization, 2018, 144: 205 − 218. DOI: 10.1016/j.matchar.2018.07.018.

[3] WANG Lei, GAO Ming, ZHANG Chen, et al. Effect of beam oscillating pattern on weld characterization of laser welding of AA6061-T6 aluminum alloy [J]. Materials & Design, 2016, 108: 707−717. DOI: 10.1016/j.matdes.2016.07.053.

[4] ZHANG Long, LI Ke, HE Hong, et al. Influence of prolonged natural aging followed by artificial aging ontensile properties and compressive behavior of a thin-walled6005 aluminum alloy tube [J]. Journal of Central South University, 2021, 28(9): 2647 − 2659. DOI: https://doi. org/10.1007/s11771-021-4799-2.

[5] de SALAZAR J M G, UREÑA A, VILLAURIZ E, et al. TIG and MIG welding of 6061 and 7020 aluminium alloys. Microstructural studies and mechanical properties [J]. Welding International, 1999, 13(4): 293−295. DOI: 10.1080/09507119909447381.

[6] YAN Shao-hua, NIE Yuan, ZHU Zong-tao, et al. Characteristics of microstructure and fatigue resistance of hybrid fiber laser-MIG welded Al-Mg alloy joints [J]. Applied Surface Science, 2014, 298: 12−18. DOI: 10.1016/j.apsusc.2013.12.157.

[7] LIANG Ying, HU Sheng-sun, SHEN Jun-qi, et al. Geometrical and microstructural characteristics of the TIG-CMT hybrid welding in 6061 aluminum alloy cladding [J]. Journal of Materials Processing Technology, 2017, 239: 18−30. DOI: 10.1016/j.jmatprotec.2016.08.005.

[8] GAUR V, ENOKI M, OKADA T, et al. A study on fatigue behavior of MIG-welded Al-Mg alloy with different filler-wire materials under mean stress [J]. International Journal of Fatigue, 2018, 107: 119−129. DOI: 10.1016/j.ijfatigue.2017.11.001.

[9] LIU Jia, ZHU Hong-yin, LI Zhong, et al. Effect of ultrasonic power on porosity, microstructure, mechanical properties of the aluminum alloy joint by ultrasonic assisted laser-MIG hybrid welding [J]. Optics & Laser Technology, 2019, 119: 105619. DOI: 10.1016/j.optlastec.2019.105619.

[10] STEEN W M. Arc augmented laser processing of materials [J]. Journal of Applied Physics, 1980, 51(11): 5636 − 5641. DOI: 10.1063/1.327560.

[11] YAN Shao-hua, CHEN Hui, ZHU Zong-tao, et al. Hybrid laser-metal inert gas welding of Al-Mg-Si alloy joints: Microstructure and mechanical properties [J]. Materials & Design, 2014, 61: 160 − 167. DOI: 10.1016/j. matdes. 2014.04.062.

[12] YAN Jun, ZENG Xiao-yan, GAO Ming, et al. Effect of welding wires on microstructure and mechanical properties of 2A12 aluminum alloy in CO_2 laser-MIG hybrid welding [J]. Applied Surface Science, 2009, 255(16): 7307 − 7313. DOI: 10.1016/j.apsusc.2009.03.088.

[13] TANG Guo, CHEN Hui, YANG Xiao-yi, et al. Effects of different welding process on the electronic temperature of plasma and weld shape during laser-MIG hybrid welding of A7N01P-T4 aluminum alloy [J]. Journal of Laser Applications, 2018, 30(2): 022002. DOI: 10.2351/1.5004434.

[14] HAN Xiao-hui, YANG Zhi-bin, MA Yin, et al. Porosity distribution and mechanical response of laser-MIG hybrid butt welded 6082-T6 aluminum alloy joint [J]. Optics & Laser Technology, 2020, 132: 106511. DOI: 10.1016/j.optlastec.2020.106511.

[15] YONETANI H. Laser-MIG hybrid welding to aluminium alloy carbody shell for railway vehicles [J]. Welding International, 2008, 22(10): 701 − 704. DOI: 10.1080/09507110802465050.

[16] PAIL K. Usability of Laser-Arc hybrid welding processes in industrial applications [D]. Finland, Lappeenranta: University of Lappeenranta Technology, 2011. https://www.researchgate.net/publication/ 266576970.

[17] OLA O T, DOERN F E. Keyhole-induced porosity in laser-arc hybrid welded aluminum [J]. The International Journal of Advanced Manufacturing Technology, 2015, 80(1−4): 3−10. DOI: 10.1007/s00170-015-6987-4.

[18] WANG Jing-bo, NISHIMURA H, FUJII K, et al. Study of improvement of gap tolerance in laser MIG arc hybrid welding of aluminium alloy [J]. Welding International, 2009, 23(10): 723−733. DOI: 10.1080/09507110902836879.

[19] ASCARI A, FORTUNATO A, ORAZI L, et al. The influence of process parameters on porosity formation in hybrid LASER-GMA welding of AA6082 aluminum alloy [J]. Optics & Laser Technology, 2012, 44(5): 1485 − 1490. DOI: 10.1016/j.optlastec.2011.12.014.

[20] WANG Lei, LIU Yao, YANG Cheng-gang, et al. Study of porosity suppression in oscillating laser-MIG hybrid welding of AA6082 aluminum alloy [J]. Journal of Materials Processing Technology, 2021, 292: 117053. DOI: 10.1016/j.jmatprotec.2021.117053.

[21] CHEN Rong, JIANG Ping, SHAO Xin-yu, et al. Effect of magnetic field on crystallographic orientation for stainless steel 316L laser-MIG hybrid welds and its strengthening mechanism on fatigue resistance [J]. International Journal of Fatigue, 2018, 112: 308−317. DOI: 10.1016/j.ijfatigue.2018.03.034.

[22] LIU Hao-bo, YANG Shang-lei, XIE Chao-jie, et al. Microstructure characterization and mechanism of fatigue crack initiation near pores for 6005A CMT welded joint [J]. Materials Science and Engineering A, 2017, 707: 22 − 29. DOI: 10.1016/j.msea.2017.09.029.

[23] DUAN Chen-feng, YANG Shang-lei, GU Jia-xing, et al. Study on microstructure and fatigue damage mechanism of 6082 aluminum alloy T-type metal inert gas (MIG) welded joint [J]. Applied Sciences, 2018, 8(10): 1741. DOI: 10.3390/app8101741.

[24] GU Jia-xing, YANG Shang-lei, XIONG Qi, et al. Microstructure and mechanical study on laser-arc-welded Al-Zn-Mg alloy [J]. Materials Transactions, 2020, 61(1): 119−126. DOI: 10.2320/matertrans.mt-m2019178.

[25] BAKER K L, WARNER D H. An atomistic investigation into the nature of near threshold fatigue crack growth in aluminum alloys [J]. Engineering Fracture Mechanics, 2014, 115: 111−121. DOI: 10.1016/j.engfracmech.2013.10.019.

[26] HUANG Yi, HUANG Jian, NIE Pu-lin. Microstructures and textures of 6016 and 5182 aluminum laser welded joints [J]. Chinese Journal of Lasers, 2019, 46(4): 50−56. (in Chinese)

[27] ZHAN Xiao-hong, ZHAO Yan-qiu, LIU Ze-min, et al. Microstructure and porosity characteristics of 5A06 aluminum alloy joints using laser-MIG hybrid welding [J]. Journal of Manufacturing Processes, 2018, 35: 437 − 445.

DOI: 10.1016/j.jmapro.2018.08.011.
[28] ZHONG Qun-peng, ZHAO Zi-hua. Fractography [M]. Higher Education Press, Beijing, 2006: 146−155. https://max.book118.com/html/2017/0419/101183533.shtm. (in Chinese)
[29] CHANG Yi-ling, HUNG F Y, LUI T S. Enhancing the tensile yield strength of A6082 aluminum alloy with rapid heat solutionizing [J]. Materials Science and Engineering A, 2017, 702: 438−445. DOI: 10.1016/j.msea.2017.07.021.
[30] QIAO Ke, WANG Kuai-she, WANG Wen, et al. Low-cycle Fatigue Properties of Friction Stir Welding Joint of AZ31 Magnesium [J]. Rare Metal Materials and Engineering, 2019, 48(3): 788−796.
[31] LIN Sen, DENG Yun-lai, TANG Jian-guo, et al. Microstructures and fatigue behavior of metal-inert-gas-welded joints for extruded Al-Mg-Si alloy [J]. Materials Science and Engineering A, 2019, 745: 63 − 73. DOI: 10.1016/j.msea.2018.12.080.
[32] ZHAO Yan-qiu, ZHOU Xu-dong, LIU Ting, et al. Investigate on the porosity morphology and formation mechanism in laser-MIG hybrid welded joint for 5A06 aluminum alloy with Y-shaped groove [J]. Journal of Manufacturing Processes, 2020, 57: 847−856. DOI: 10.1016/j.jmapro.2020.07.044.
[33] FENG Lei, XUAN Fu-zhen. Effect of non-metallic inclusions on the local stress concentration within materials [J]. Journal of Mechanical Engineering, 2013, 49(8): 41−48. DOI: 10. 3901/JME.2013.08.041. (in Chinese).
[34] MUGHRABI H. Specific features and mechanisms of fatigue in the ultrahigh-cycle regime [J]. International Journal of Fatigue, 2006, 28(11): 1501−1508. DOI: 10.1016/j.ijfatigue.2005.05.018.

(Edited by HE Yun-bin)

中文导读

6061铝合金激光-MIG复合焊接头的组织与力学性能

摘要：本文采用激光-MIG复合焊接技术对3 mm的6061铝合金板材进行焊接。在实验的基础上，确定了最佳的焊接工艺参数，保证了熔透焊接。采用光学显微镜(OM)、扫描电镜(SEM)和能谱仪(EDS)对焊接接头的微观组织、拉伸和疲劳断口形貌以及表面疲劳损伤进行分析。结果表明，焊接接头中存在两种主要析出相，一种是晶界长的富Si沉淀相，另一种是晶内富Cu沉淀相。拉伸试验结果表明，接头的抗拉强度为224 MPa，仅为母材的70.2%。通过对拉伸断口的分析，发现母材与接头拉伸韧窝的形成有很大差异。在应力率为0.1的拉−拉疲劳试验中，母材和焊接接头的条件疲劳极限分别为101.9和54.4 MPa。通过对比不同应力幅下焊接接头的疲劳断口，发现导致接头断裂的主要因素是气孔。通过对孔隙缺陷的进一步分析，发现孔隙中微裂纹的扩展方式有穿晶和沿晶两种，并存在二者混合扩展方式。

关键词：铝合金；激光-MIG复合焊接；疲劳性能；微观组织；力学性能